PROCEEDINGS OF SCIENCE

Diffuse emission study with INTEGRAL/SPI after 10 years of observations: preliminary mapping of the ^{26}Al emission

Laurent Bouchet*, **Elisabeth Jourdain, Jean-Pierre Roques**
Université de Toulouse, UPS-OMP, IRAP, Toulouse, France
CNRS, IRAP, 9 Av. colonel Roche, BP 44346, F-31028 Toulouse cedex 4, France
E-mail: lbouchet@irap.omp.eu

The SPI spectrometer is currently the most sensitive instrument operating in the MeV energy region. We take advantage of the long sky exposure duration ($\sim 2\times10^8$s) obtained between 2003 and 2013 to map the large scale structure morphologies of the Galaxy. We emphasis the ^{26}Al radioactive line emission. So far, only *COMPTEL* data have allowed to perform its detailed morphology study. The *INTEGRAL* mission is an opportunity to provide additional information on this topic. We developed a maximum entropy code to attempt to reconstruct the image of the sky. The preliminary map shows that the emission comes mainly from the inner Galaxy region, and hence supports the chief findings of *COMPTEL*. The map also indicates more localized potential sites of emission.

10th INTEGRAL Workshop: A Synergistic View of the High-Energy Sky
15-19 September 2014
Annapolis, MD, USA

*Speaker.

PoS(Integral2014)055

1. Introduction

The SPI telescope on the *INTEGRAL* observatory is currently the only instrument operating around the MeV region. Thanks to its imaging capabilities, the telescope is able to disentangle the spatial morphology and the spectral shape of the various emission components; each one is linked to specific physical processes. Using SPI data, only the morphologies study of the diffuse continuum ([3]) and the 511 keV electron-positron line ([4, 5, 6]) have been performed.
However, to date, only the *COMPTEL* Compton telescope aboard the *Compton Gamma Ray Observatory* has mapped the ^{26}Al during its nine years survey. The emission has been found mainly distributed along the Galactic plane and supports a massive-stars origin ([7, 8, 9, 10]). In addition, the early *COMPTEL* sky maps suggest many potential marginally significant spots, some of them being potentially associated with the Galactic spiral arms structure [11]. However, while the main features of the *COMPTEL* map are set with confidence, the low-intensity features, which depend on the data analysis method, need to be confirmed.
These *COMPTEL* maps have been used as a basis to fix the spatial morphology of the ^{26}Al line emission for subsequent works related to the spectral analyzes. Among them, detailed studies in the inner Galaxy and extended regions along the Galactic plane made with SPI indicates that the intrinsic line width is less than 1.3 keV and that line position shifts along the plane correspond to the rotation of our Galaxy, confirming at least a partial association of the ^{26}Al emission with the spiral arms ([12, 13, 14]).
In this paper, 10 years of *INTEGRAL* observation are used to attempt to examine the spatial morphology of the ^{26}Al line, through direct sky-imaging and sky distribution model comparison. We emphasis on the data analysis, especially the instrumental background modeling issue, a key point for both *COMPTEL* and SPI instruments. We also present the preliminary results based on a phenomenological modeling of the background and a maximum entropy method image reconstruction algorithm.

2. Instrument and observations

The SPI spectrometer ([15, 16]) observes the sky in the 20 keV to 8 MeV range. In addition to its spectroscopic capabilities, SPI can image the sky with a spatial resolution of $\sim 3^\circ$ (FWHM) over a field-of-view of 30° thanks to a coded-mask aperture. A revolution lasts 3 days, the time that the spacecraft performs a large eccentric orbit, but half a day of data is unusable because of the radiation belts crossing. Then a revolution contains generally about 100 exposures lasting approximately 45 minutes each. The analysis presented in this paper is based on the data obtained between 2003 and 2013 single-events, which represent $\sim 2\times 10^8$s of observations after the filtering of the data.

3. Analysis

The signal recorded by the SPI camera on the 19 Ge detectors is composed of contributions from each source (point-like or extended) present in the field of view, convolved by the instrument aperture, plus the background. To determine the sky model parameters, we adjust the data through

a multi-component fitting algorithm, based on the maximum likelihood statistics. We use the Cash [17] statistics, but we present the results in term of the equivalent chi-square statistics (χ^2_L). The core algorithm developed to handle such a large system is described in [18]. The analysis performed in this paper will be described in more detailed in [19], we remind here the main points.

3.1 Background determination

The instrumental background is the main contributor to the flux recorded by the detector plane and a key issue since the signal-to-noise ratios considered in this study are below 1%.
For N_p exposures and N_d detectors, the background term, formally consisting of $N_d \times N_p$ values (one per detector and per pointing) can be rewritten as:

$$b_{dp} = a_p \times u_d \times t_{dp} \tag{3.1}$$

Here u is a vector of N_d elements, representing the "uniformity map" of the detector plane (background pattern), t_{dp} the effective observation time for detector d and pointing p. The evolution of the background intensity is traced with a_p, a scalar normalization coefficient per pointing. Fortunately, the background intensity (a_p) does not necessarily vary so rapidly and the number of related background parameters could be still decreased, according to the actual background evolution.

3.2 Background intensity variations

We have applied a segmentation algorithm, developed to determine the variability timescale of the sources ([20]), to the background signal. We first subtracted the source contribution to the total counts. A rough approximation of the sky signal is enough for this purpose (its contribution to the total counts is weak). Then, for each exposure, counts are summed over all detectors, and for each revolution, the corresponding time-series (up to one hundred of exposures) is segmented. The number of segments and their lengths are adjusted in order to obtain the minimal number of segments ensuring $\chi^2/\mathrm{dof} \leq 1$. The background intensity has been found stable (fit with one segment) during 44% of the revolutions. Finally, the total number of segments has been significantly reduced since only $\sim$3 000 segments are required, instead of the $\sim$12 000 segments used when fixing a $\sim$6 hours timescale. Finally, these (model-independent) time segments have been used to describe the background evolution in our subsequent analyzes.

3.2.1 "Uniformity map"

The uniformity map or background pattern u in Equation 1 can be hand fixed before the fitting procedure by using "empty-field" observations. The dedicated SPI "empty-field" observations are rare, but the exposures whose pointing latitude direction satisfies $|b| > 30^\circ$ constitute a good approximation since they contain only weak contributions from sources, at the energies considered here. They amount to 20% of the observations and have been used for building a set of background templates for different periods along the mission (about one per 6 months).
To quantify the properties of the background pattern for each period, we define the vector u as

$$u(d) = \frac{\sum_p d_p(d)}{\sum_p t_p(d)} \text{ for exposure p satisfying } |\mathrm{b}| \geq 30^\circ \tag{3.2}$$

However, in the case of a diffuse emission, the high-latitude exposure fields may contain some signal and the background pattern deduced from them may be "blurred". In addition, for the ^{26}Al study, we have to keep in mind that the side shields do not stop 100% of photons. This means that any uniformity map or background pattern will contain also some diffuse emission signal passing through the shield.
Therefore, we have investigated another approach to estimate the detector uniformity pattern, by fitting it during the convergence procedure. However, this improvement is not fully reliable enough since the recovered source signal becomes background dependent and can be altered to an extent which is difficult to estimate.
The two pattern determination methods are subsequently referred to as fixed-pattern and fitted-pattern ones and we have systematically compared the results obtained with each of them.

4. Imaging

To build an image, the sky is divided into small areas or pixels, the flux f in each pixel is being to be determined. The linear model of the data is

$$n = Rf + b + \varepsilon \tag{4.1}$$

n represents the data, b the background, R the response of the instrument and ε the instrumental noise. n, b and ε are vectors of length M (the number of data points), f a vector of length N (the number of pixels in the sky) and R a matrix of size M by N. The instrumental noise is assumed to follow a Gaussian distribution with a variance σ^2 and a null mean.
However, when the number of pixels is large, the system of equations is ill-conditioned. The most common technique consists in including a regularization term on the solution (term H) in addition to the goodness of the fit (χ^2) constraint. The function to maximize is then,

$$Q(f) = \alpha H(f) - \frac{1}{2}\chi^2(f) \tag{4.2}$$

where α is a parameter, which determines the degree of smoothing of the solution.
We choose to used one of the most popular regularization operators: the entropy function. This method is known as the Maximum-Entropy Method or MEM ([21] and references therein). For an assumed positive additive distributions,

$$H(f) = \sum_{i=1}^{N} f_i - m_i - f_i log\frac{f_i}{m_i} \tag{4.3}$$

where m_i is the default initial value assigned to the pixel i. The pixel flux f_i and m_i are positive quantities. In our application, the instrumental background variation timescale is fixed through the modeling method presented in Section 3.2. We search for both the solution vector f (length N) and the intensities of the background b (length N_b).
We introduce artificially the possible correlations between the pixels of the image (the sky emission should vary smoothly from one pixel to the next ones) by using an Intrinsic Correlation Function, ICF ([21]),

$$Q(f) = \alpha H(f) - \frac{1}{2}\chi^2(f_{ICF}) \text{ where } f_{ICF} \equiv ICF(f) \tag{4.4}$$

We chose a radial Gaussian function as ICF function.

5. Results

The image displayed in Figure 1 indicates that the emission is essentially confined in the inner Galaxy region ($|l| \leq 30°$, $|b| \leq 10°$) with a corresponding estimated flux of $\sim 3.5 \times 10^{-4}$ph cm^{-2} s^{-1} .

Beyond the morphology of the diffuse emission, there are several spots visible in the image. Indeed, some of them have positions compatible with sources detected or studied during recent SPI investigations ([23, 24, 25]).

In the Cygnus region ($72° < l < 96°$, $-7° < b < 7°$), the image reveals also several excesses. A significant one is located at a position compatible with Cyg OB2 cluster (81°,-1°) as reported by [23].

The strongest excess visible in Sco-Cen region ($328° < l < 355°$, $8° < b < 30°$) is localized at (l, b) ≈(360°, 16°), with a spatial extent around 5° radius. This position remain compatible with the position (l,b)=(350°,20°) and a spatial extension of 10° radius reported in [24].

There are also some structures around Carina and Vela region and two extended structures appear in the Taurus/Anticenter region ($105° < l < 170°$, $-15° < b < 20°$). In addition, a spot is worth to be mentioned since it is detected above 3 σ, at high-latitude (l,b)≈(226°,76°) with a flux of $(7 \pm 2) \times 10^{-5}$ photons cm^{-2} s^{-1}, for which we did not find any convincing potential counterpart.

A template comparison analysis similar to the one done for the *COMPTEL* data ([9]) has been performed. It consist of using template maps to model the spatial distribution of the the ^{26}Al emission through the Galaxy. To obtain the detection significance of the ^{26}Al using a given template, we adjust two models to the data, the first one contains only the background while the second contains the background plus a template map (Table 1). For the fixed-pattern method, this leads to a ^{26}Al detection significance of $\sim 23\sigma$ with a $\chi^2_L/dof = 1.004$. In addition, each template is significantly detected, the worse template (H_I) has a significance of $\sim 17\sigma$. The same analysis for the fitted-pattern pattern gives a^{26}Al detection significance of $\sim 18\sigma$ with a $\chi^2_L/dof = 0.997$.

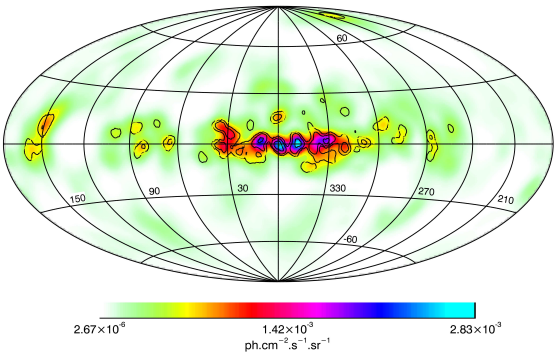

Figure 1: Image of the ^{26}Al line (1805-1813 keV). The resolution of the image is 6° (ICF of 6° FWHM). The contours are extracted from the 3° resolution image, in units of $\times 10^{-3}$ ph cm^{-2} s^{-1} sr^{-1}, they correspond to 0.6, 1.3, and 3.2. The yellow contours is indicates the level 0.6×10^{-3} ph cm^{-2} s^{-1} sr^{-1} of the 6° image. From left to right: Perseus region ($105° \leq l \leq 170°$) (Taurus clouds), the Cygnus/Cepheus region ($75° \leq l \leq 100°$), the inner Galaxy ($-30° \leq l \leq 30°$, $-10° \leq b \leq 10°$), Carina (l=286°, b=1°) and Vela region ($260° \leq l \leq 270°$). At mid-latitude, the Sco/Cen region ($300° \leq l \leq 360°$, $8° \leq b \leq 30°$).

As shown on Figure 2, the reconstructed flux attributed to the inner Galaxy does not depend much on the template map and is compatible with a value of 3.3×10^{-4} ph cm^{-2} s^{-1} , in agreement with the previously reported values. However, the total flux integrated over the whole sky clearly depends on the contrast of the assumed model. The contrast is defined as the ratio of the flux contained in the region $|l| \leq 150°$, $|b| \leq 15°$ to the total flux enclosed in $|l| \leq 180°$, $|b| \leq 90°$. The more

Table 1: Maps used as templates.

	Tracer	Mechanism
†MIR 12 and 25μ	warm dust (T$\sim$250 and $\sim$120 K)/AGBs	dust nano-grains and PAHS heated to high temperature
†53 GHz sync	cosmic-rays/magnetic field	Synchrotron
[a]*COMPTEL*-MEM IC	Inverse-Compton from GeV electrons on the CMB/ISRF	Inverse-Compton
†NIR 1.25,4.9 μ	stars (K and M giants)	star light
[b]H_I (21 cm)	H hyperfine transition	Neutral hydrogen
†NIR 2.2μ	stars (K and M giants)	star light
†EGRET	Interstellar gas/cosmic-rays	nuclear interactions
†NIR 3.5 μ	stars (K and M giants)	star light
†53 GHz free-free	ionized gas	Free-free
†53 GHz dust	dust	Thermal dust
†FIR 100, 140 and 240μ	warm dust (T $\sim$30, $\sim$21 and $\sim$12 K)	microns sized dust emitting in thermal equilibrium with the heating ISRF
[a]*COMPTEL*-MREM †FIR 60μ	warm dust (T$\sim$50 K)	microns sized dust emitting in thermal equilibrium with the heating ISRF
[c]CO	CO rotational transition	Molecular gas / young stars
[d]NIR extinction-corrected map 3.5 and 4.9 μ hereafter ($\mathbf{A}_{4.9\mu}$ and $\mathbf{A}_{3.5\mu}$)	stars (K and M giants)	star light

The maps are ordered in ascending "contrast", defined here as the ratio between the fraction of the emission enclosed in the region $|l| < 150°$, $|b| < 15°$ to that of the whole sky. The value of the ratio varies from 0.4 (25μ) to nearly 1 ($\mathbf{A}_{4.9\mu}$). † available at http://lambda.gsfc.nasa.gov.

[a] The maximum-entropy (MEM) and Multi-resolution Regularized Expectation Maximization (MREM) all-sky image of the Galactic 1809 keV line emission observed with *COMPTEL* over 9 years ([10] and references therein). [b][30]. [c][31]. [d]The NIR extinction maps, the employed correction of course removed only main effects of interstellar extinction on the DIRBE map ([32] and references therein), and the resulting maps are not expected to have an accuracy higher than $\sim$10%.

the map is contrasted (from left to right on Figure 2, the weaker is the reconstructed total flux. This is due to the fact that the recovered global intensity relies on the central parts of the image (both higher flux and signal to noise ratios) and that a contrasted map encompasses less flux in its external parts than a flatter map Figure 2 displays the Maximum Likelihood Ratio (MLR) obtained with both pattern determination methods (fixed and fitted-pattern) for each of the tested maps (ordered

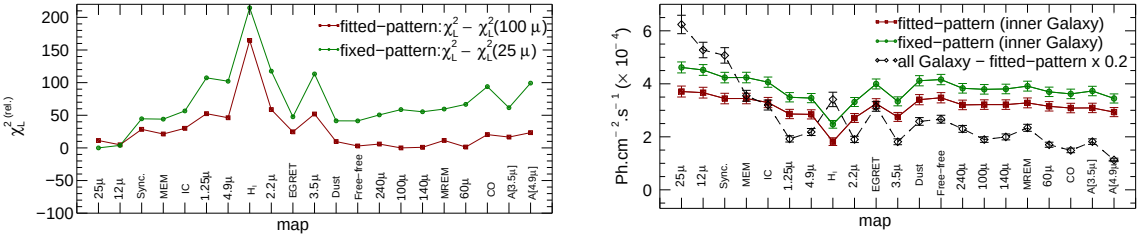

Figure 2: The maps are ordered following their contrast defined as the ratio of the flux enclosed in the region $|l| < 150°$, $|b| < 15°$ to the total flux. Terms sync., dust and free-free, are abbreviations for 53 GHz synchrotron, dust and free-free maps. MEM and MREM indicate the *COMPTEL* maps, A[3.5μ] and A[4.9μ]corrected NIR extinction map. The red curve is for the fitted pattern and green for fixed pattern method. **Left**: The relative chi-square variation ($\chi_L^{2(rel.)}$)) versus assumed template to model the distribution of the ^{26}Al line. $\chi_L^{2(rel.)}$) is the χ_L^2 from which the value of the best fitted template is subtracted. The best template is the 100μ template for the fitted-pattern method. and the 25μ template for the fixed-pattern method. **Right**: Flux in the inner Galaxy in function of the map used to model the distribution of the ^{26}Al line. The dashed black-curve is the total flux in the Galaxy (fitted-pattern), scaled by a factor 0.2.

by increasing contrast). Several maps lead to similar results and we could say that star related distributions (FIR and MIR maps, dust and free-free distributions, all with rather high-contrast) give a good description of the data, as expected from what we know about the ^{26}Al emission process. Similarly, 25μ and 12μ maps constitute good tracers, while presenting a low-contrast. In other hand, H_I and 53 GHz synchrotron maps can be excluded. In fact, we have seen (Figure 1) that the emission is confined into the central part of the Galaxy. This explains why the H_I map does not provide a good fit to the data since it extends far in longitude and contains important emission at $|l| \geq 30°$. We also note that distributions built by imaging method (MEM or MREM from *COMPTEL* data) remain good tracers of the ^{26}Al emission.
We note that the chi-square curves follows the same evolution regardless the background determination method and hence that the conclusions do not depend much on it.

6. Summary

For more than a decade, the reference map for the spatial morphology of the ^{26}Al emission was provided by *COMPTEL*. The emission has been found to be confined essentially to the inner Galaxy. Indeed, the first MEM images ([7, 8]) exhibits many low-intensity structures. A small number of them remain in the latest MEM image ([10]), giving some confidence about their reality. In parallel, the chief features of these MEM images were confirmed with a MREM algorithm ([33]).
In the model fitting analysis based on other wavelength maps, our data do not allow us to distinguish a unique template since several one lead to similar likelihood parameter. From *COMPTEL* data, [9] had concluded that the best tracers were DIRBE 240μ and 53 GHz free-free maps. We agree that the FIR maps with wavelengths 60 to 240 μ or 53 GHz (free-free and dust) appear to give statistically the best estimate of the ^{26}Al emission global morphology but CO, NIR A[4.9μ] and A[3.5μ] extinction-corrected maps have also to be considered with only a slightly lesser degree of confidence. In addition, "low-contrast" maps observed at 25μ and 12μ provide an equally good

description of the emission.

Indeed, our results confirm that the ^{26}Al emission follows more or less the distribution of the extreme Population *I*, the most massive stars in the Galaxy ([7]). It is known that the massive stars, supernovae and novae produce the long-lived isotopes ^{26}Al and ^{60}Fe with half-lives of 0.7 and 2.6 My. In addition, core collapse SNe produce dust/grains while massive star-supernovae are major dust factories, therefore dust FIR and MIR maps are expected to provide a good description of the emission. Quantitatively, the flux extracted through the model fitting method for the inner Galaxy $|l| \leq 30^\circ$,$|b| \leq 10^\circ$ is found to be around $3.3\times\ 10^{-4}$ph cm^{-2} s^{-1} while it does not depend much on the sky model (particularly if we restrict ourselves to the preferred ones). Similarly, [6] using a light-bucket" method obtain a flux $4\ \times\ 10^{-4}$ ph cm^{-2} s^{-1} for the region delimited by $|l| \leq 40^\circ$,$|b| \leq 40^\circ$. For the same region, we obtain a flux of $\sim 3.9\ \times\ 10^{-4}$ph cm^{-2} s^{-1} with the most probable spatial morphologies. Our measured flux is consistent with earlier measurements of both *INTEGRAL*/SPI and *COMPTEL* instruments. Another observable quantity, related to ^{26}Al production is the ratio between ^{60}Fe and ^{26}Al line fluxes in the inner Galaxy. With our analysis, the ^{60}Fe mean flux in the inner Galaxy is about $4\times\ 10^{-5}$ photons cm^{-2} s^{-1}, leading to a ^{60}Fe to ^{26}Al ratio between 0.12 and 0.15. Considering the numerous uncertainties still affecting these models, this results confirms those reported by [28, 34], and can be used to reject some hypotheses, but not yet to definitively discriminate the good ones.

We performed a direct imaging reconstruction of the ^{26}Al emission by using maximum-entropy method. The code is based on [29] algorithm. The resulting SPI image presented in Figure 1 resembles the MEM *COMPTEL* images in term of angular resolution and details. With a resolution fixed to $\sim$6°, it gives essentially the same information as the previous method, e.g. the emission is confined in the inner-Galaxy disk. But, it also suggests the presence of extended (a few degrees) emitting areas. Several excesses appear in both SPI and *COMPTEL* data analyzes of [10] which reinforces their reliability.

The Cygnus complex is seen in the *COMPTEL* images. We report for Cyg OB2 cluster a flux of $4.1-4.5\pm1.5\times\ 10^{-5}$ photons cm^{-2} s^{-1} compatible with the value of $3.9\pm1.1\times\ 10^{-5}$ photons cm^{-2} s^{-1} reported by [23].

The Vela and Carina regions, although their flux are comparable to the estimations reported for Carina [25] and for Vela (*COMPTEL* data; [35]) are detected at low significance level (2σ).

The image shows an excess compatible with Sco-Cen region. This excess was detected with a high confidence level (the flux is $6\pm1\times\ 10^{-5}$ photons cm^{-2} s^{-1}) with the somewhat different analysis of [24] using SPI data. We report by using the same spatial extension and location as in [24] a maximum flux of $(4.2\pm1.6)\times\ 10^{-5}$ photons cm^{-2} s^{-1} and by using the spatial extent and location which are based on our image analysis, which stays compatible with the one assessed by [24], a flux of ($4.1\pm1.6\times\ 10^{-5}$ photons cm^{-2} s^{-1}). However, the model-fitting analysis shows that the measured flux depends on the template, which is used to model the large-scale emission of the ^{26}Al line (it is detected only above 2σ with an H$_I$ template). We note that this feature is not reported by the *COMPTEL* data analysis.

We have two significant and robust excesses, not previously reported by *COMPTEL*. These excesses, rather extended, are seen in the Taurus/Anticenter region at (l,b)$\simeq$ (161°,-3°) and (l,b)$\simeq$ (149°, 8°) with fluxes of $4-6\pm2$ and $8-9\pm3\times\ 10^{-5}$ photons cm^{-2} s^{-1}. We wanted to mention an excess at high-latitude ($(7\pm2)\times\ 10^{-5}$ photons cm^{-2} s^{-1}) not previously reported.

A more direct comparison of SPI and *COMPTEL* data shows that the ^{26}Al line is detected at $\sim 20\sigma$ using SPI data which is to be compared to the $\sim 30\sigma$ obtained with the analysis of *COMPTEL* data ([9]). The point-source (3 σ) is $1.4\times\ 10^{-5}$ photons cm^{-2} s^{-1}in the Galactic center region to be compared to the 0.8 to $1.4\times\ 10^{-5}$ photons cm^{-2} s^{-1}reported by [10] for *COMPTEL*.
Finally, in addition to Cygnus feature, the SPI image indicates important spots at l$\simeq$330° and l$\simeq$320° and two features, which we tentatively associated to Taurus/Anticenter region. This could be correlated to MREM image, for which it is mentioned in addition to Cygnus feature, two spots at l$\simeq$317 degrees and l$\simeq$332 degrees and an extended emission around (l, b) $\simeq$(160°,0°).
Some improvements in the data analysis appear achievable to still refine our results. In particular, an accurate modeling of the response outside the field of view is a prime objective for studying emissions above $\sim$ 1 MeV.

References

[1] Strong, A. W. & Moskalenko, I. V., 1998, *ApJ* , 509, 212

[2] Porter, T. A., Moskalenko, I. V., Strong, A. W., et al., 2008, *ApJ* , 682, 400

[3] Bouchet, L., Strong, A., Porter, T.A, et al., 2011, *ApJ* , 739, 29

[4] Weidenspointner, G., Skinner, G., Jean, P., et al., 2008, *Nature*, 451, 159

[5] Bouchet, L., Roques, J. P. & Jourdain, E., 2010, *ApJ* , 720, 177

[6] Churazov, E., Sazonov, S., Ysygankov S., et al., 2011, *MNRAS*, 411, 1727

[7] Diehl, R., Bennett, K., Bloemen, et al., 1995, *A & A* , 298, L25

[8] Oberlack, U., Bennett, K., Bloemen, H., et al., 1996, *A & A sup. series*, 120, 311

[9] Knödlseder, J., Bennett, K., Bloemen, H., et al., 1999, *A & A* , 344, 68

[10] Plüschke, S., Diehl, R., Schoenfelder, V., et al., Proceedings of the Fourth INTEGRAL Workshop, ESA SP-459, 2001

[11] Chen, W., Gehrels, N., Diehl, R. and Hartmann, D., 1996, A&AS, 120, 315

[12] Diehl, R., Halloin, H., Kretschmer, K., et al., 2006, *Nature*, 439, 435

[13] Wang, W., Lang, M. G., Diehl, R., et al., 2009, *A & A* , 496, 713

[14] Kretschmer, K., Diehl, R., Krause, M. et al., 2013, aap, 559, 99

[15] Vedrenne, G., Roques, J. P., Schonfelder, V., et al., 2003, *A & A* , 411, L63

[16] Roques, J. P., Schanne, S., Von Kienlin, A., et al., 2003, *A & A* , 411, L91

[17] Cash, W., 1979, *ApJ* , 228, 939

[18] Bouchet, L., Amestoy, P., Buttari, A, Rouet, F.-H. and Chauvin, M., 2013a, Astronomy and Computing, Volume 1, 59

[19] Bouchet, L., Roques, J. P. & Jourdain, E., in preparation, 2015

[20] Bouchet, L., Amestoy, P., Buttari, A, Rouet, F.-H. and Chauvin, M., 2013, *A & A* , 555, 52

[21] Gull, S. F., 1989, in Skilling J., ed., Maximum Entropy and Bayesian Methods. Kluwer, Dordrecht, p. 53

[22] Skilling, J., 1981, Workshop on Maximum Entropy Estimation and Data Analysis, University of Wyoming, Reidel, Dordrecht, Holland

[23] Martin, P., Knödlseder, J., Diehl, R. & Meynet G., 2009 *A & A* , 506, 703

[24] Diehl, R., Lang, M.G., Martin, P. et al., 2010, *A & A* , 522, A51

[25] Voss, R., Martin, P., Diehl, R., et al., 2012, *A & A* , 539, 66

[26] Knodlseder99 Knödlseder, J., Bennett, K., Bloemen, H., et al., 1999, *A & A* , 344, 68

[27] Knödlseder, J., Weidenspointner, G., Jean, P. et al., 2006, The Obscured Universe. Proceedings of the VI INTEGRAL Workshop, Editor: S. Grebenev, R. Sunyaev, C. Winkler. ESA SP-622, Noordwijk: ESA Publication Division, ISBN 92-9291-933-2, p 13

[28] Harris, M. J, Knödlseder, J., Jean, P., et al., 2005, *A & A* , 433, L49

[29] Skilling, J. & Bryan, R. K., 1984, *MNRAS*, 211, 111

[30] Dickey, J. M., & Lockman, F. J. 1990, ARA&A , 28, 215

[31] Dame, T. M., Hartmann, D. and Thaddeus, P., 2001, *ApJ* , 547, 792

[32] Krivonos, R., Revnivtsev, M., Churazov, E., et al., 2007, *A & A* , 463, 957

[33] Knödlseder, Dixon, D., J., Bennett, K., et al., 1999, *A & A* , 345, 813

[34] Wang, W., Harris, M. J., Diehl, R., et al., 2007, *A & A* , 469, 1005

[35] Diehl, R., Bennett, K., Bloemen, et al., 1995a, *A & A* , 298, L25